Monthly Notices of the ROYAL ASTRONOMICAL SOCIETY

MNRAS **462,** 4473–4481 (2016) doi:10.1093/mnras/stw1860
Advance Access publication 2016 July 30

The missing satellite problem in 3D

A. M. Nierenberg,[1⋆†] T. Treu,[2‡] N. Menci,[3] Y. Lu,[4] Paul Torrey[5,6] and M. Vogelsberger[5]

[1]*Center for Cosmology and AstroParticle Physics, The Ohio State University, Columbus, OH 43204, USA*
[2]*UCLA Physics & Astronomy, 475 Portola Plaza, Los Angeles, CA 90095-1547, USA*
[3]*NAF – Osservatorio Astronomico di Roma, via di Frascati 33, I-00040 Monteporzio, Italy*
[4]*Carnegie Observatories, 813 Santa Barbara Street, Pasadena, CA 91101, USA*
[5]*MIT Kavli Institute for Astrophysics and Space Research, 77 Massachusetts Ave. 37-241, Cambridge MA 02139, USA*
[6]*California Institute of Technology, Pasadena, CA 91125, USA*

Accepted 2016 July 25. Received 2016 July 25; in original form 2016 March 3

ABSTRACT

It is widely believed that the large discrepancy between the observed number of satellite galaxies and the predicted number of dark subhaloes can be resolved via a variety of baryonic effects which suppress star formation in low-mass haloes. Supporting this hypothesis, numerous high-resolution simulations with star formation and associated feedback have been shown to reproduce the satellite luminosity function around Milky Way-mass simulated galaxies at redshift zero. However, a more stringent test of these models is their ability to simultaneously match the satellite luminosity functions of a range of host halo masses and redshifts. In this work, we measure the luminosity function of faint (sub-Small Magellanic Cloud luminosity) satellites around hosts with stellar masses $10.5 < \log_{10}M_*/\mathrm{M}_\odot < 11.5$ to an unprecedented redshift of 1.5. This new measurement of the satellite luminosity function provides powerful new constraining power; we compare these results with predictions from four different simulations and show that although the models perform similarly overall, no one model reproduces the satellite luminosity function reliably at all redshifts and host stellar masses. This result highlights the continued need for improvement in understanding the fundamental physics that governs satellite galaxy evolution.

Key words: galaxies: dwarf – galaxies: evolution – galaxies: luminosity function, mass function – dark matter.

1 INTRODUCTION

One of the significant discrepancies between Λ cold dark matter (CDM) and observation is the apparent lack of structure on sub-galactic scales. This 'missing satellite problem' (Klypin et al. 1999; Moore et al. 1999) was first observed in the Local Group and has subsequently been observed in the mass function of isolated field galaxies (Papastergis et al. 2011).

One commonly adopted solution to the missing satellite problem in the context of CDM is that there are a large number of low-mass dark matter subhaloes that do not have detectable stars or gas. The key to this solution is developing a comprehensive understanding of star formation in low-mass haloes. Simulations are now able to invoke a variety of mechanisms including UV heating during reionization, supernova feedback, stellar winds, and tidal and ram pressure stripping by the host halo in order to reproduce the observed luminosity function of Milky Way satellites down to low masses at redshift zero (e.g. Thoul & Weinberg 1996; Gnedin 2000; Kaufmann et al. 2008; Macciò et al. 2010; Springel 2010a; Guo et al. 2011a; Zolotov et al. 2012; Brooks et al. 2013; Starkenburg et al. 2013; Wetzel et al. 2016). Presently, the baryonic solution to the missing satellite problem around Milky Way-like galaxies is not unique, with a variety of models all matching the data reasonably well. Much more information can be gained by comparing with observations of satellites around host galaxies of varying stellar mass and at a range of redshifts. Such a comparison can help distinguish between the roles of environmental and internal processes in regulating star formation in satellite galaxies.

It is also possible that the missing satellite problem is due to incorrect assumptions about dark matter. For instance, if dark matter is warm or significantly self-interacting, small-scale structure can

⋆E-mail: nierenberg.1@osu.edu
† CCAPP Fellow.
‡ Packard Fellow.

be erased at early times either due to finite particle velocities in the former case (e.g. Colombi, Dodelson & Widrow 1996, and references therein) or via a combination of dark sector Silk-damping and acoustic oscillations in the latter (Cyr-Racine et al. 2016; Vogelsberger et al. 2016). It is interesting to explore how different dark matter scenarios affect the star formation physics required to reproduce the observed luminosity function relative to the CDM case.

Recent observations have generated a wealth of new information about satellite galaxies at low redshift, generating new constraints for models of satellite galaxy formation and evolution. Notably, these low-redshift studies have found a significant dependence between the satellite luminosity function and host stellar mass and colour (e.g. Guo et al. 2011a; Lares, Lambas & Domínguez 2011; Liu et al. 2011; Nierenberg et al. 2012; Strigari & Wechsler 2012; Wang & White 2012; Lan, Ménard & Mo 2016; Ruiz, Trujillo & Mármol-Queraltó 2015; Sales et al. 2015). Simulations have had varying success at reproducing these trends. For instance, Wang & White (2012) found that the Guo et al. (2011b) semi-analytic model applied to Millennium II haloes matched some of the trend of increasing satellite numbers with host stellar mass, but significantly overpredicted the number of satellites around $\sim 10^{11.5}$ $M_\odot$ hosts relative to observations, as well as the number of bright satellites around lower stellar mass hosts.

Redshift provides another important dimension, in addition to host mass and colour along which to constrain star formation models, as different star formation processes occur on a broad range of time-scales. Recent studies have begun to measure the number of satellites around higher redshift hosts between redshift of 0.4 and 2 (Newman et al. 2012; Nierenberg et al. 2012; Tal et al. 2014). Nierenberg et al. (2013b) compared the measurement of the satellite luminosity function in bins of both redshift from 0.1 to 0.8 and host stellar mass to theoretical predictions from Guo et al. (2011b), Lu et al. (2012) and Menci, Fiore & Lamastra (2012), finding that although all the models matched the luminosity function of Milky Way satellites, they each predicted significantly different luminosity functions in the other host mass and redshift regimes, demonstrating the power of comparing to observations outside of the Local Group.

In this work, we extend our observation of the satellite luminosity function to fainter satellites and higher redshifts using deep, near-infrared (near-IR) imaging from Cosmic Assembly Near-infrared Deep Extragalactic Legacy Survey (CANDELS; Grogin et al. 2011; Koekemoer et al. 2011). With the power of near-IR images, we are able to double our redshift baseline (from redshift 0.8 to 1.5) and reach an order-of-magnitude fainter satellites at $z = 0.8$, with respect to our previous work. We combine the new measurement with lower redshift results from Nierenberg et al. (2012, hereafter N12), and compare these results with four state-of-the-art simulations. The models are (1) a CDM merger tree simulation with semi-analytic star formation (Menci et al. 2014), (2) a warm dark matter (WDM) merger tree with the same semi-analytic star formation implementation as in the CDM case also by Menci et al. (2014), (3) a CDM *N*-body simulation with Bayesian-tuned semi-analytic star formation from Lu et al. (2014) and (4) Illustris which is a CDM *N*-body simulation with hydrodynamical star formation (Vogelsberger et al. 2014b).

For the observational results, we assume a flat ΛCDM cosmology with $h = 0.7$ and $\Omega_m = 0.3$. We note that although these values are slightly different from those used in each of the simulations, the variations caused by adjusting these parameters are much smaller than the measurement uncertainties. All magnitudes are given in the AB system (Oke 1974).

2 DATA

To study the properties of satellites at a wide range of redshifts, we combine data from the COSMOS field (Scoville et al. 2007) and the CANDELS fields. The relatively wide COSMOS survey has ∼1.7 square degrees of *Hubble Space Telescope* (*HST*) *F*814 imaging, and is useful for constraining the satellite luminosity function at lower redshift and for higher stellar mass hosts. All results from COSMOS *I*814 imaging in this work are taken from N12 which contains a detailed discussion of the data that was used.

CANDELS has ∼0.25 square degrees of deep, near-IR *F*160*W*, *F*140*W* and *F*125*W* *HST* imaging which enables the detection of fainter satellite galaxies at higher redshifts than COSMOS. To detect satellites in CANDELS, we make extensive use of data products provided by the 3D-HST team (Brammer et al. 2012; Skelton et al. 2014), which include reduced *HST* imaging as well as photometric, stellar mass and redshift catalogues.

2.1 Host galaxy selection

We study satellites around host galaxies with stellar masses $10.5 < \log_{10}[M^*/M_\odot] < 11.5$ between redshifts $0.1 < z < 1.5$, using the stellar mass and redshift catalogues from the 3D-HST survey for CANDELS, and from Ilbert et al. (2009) and Lilly et al. (2007) for COSMOS. The host stellar mass limits were selected to ensure sufficient signal of at least ∼ one satellite per host on the low-mass end and a well-constrained halo mass-to-stellar mass relation on the higher mass end. The latter restriction is important because we select satellites based on R_{200} of the hosts. Where possible, spectroscopic redshifts were used, otherwise photometric redshifts were used from Ilbert et al. (2009) in COSMOS, and from 3D-HST photometric catalogues in CANDELS for objects with photometric redshift quality indicator $Q_z < 3$ as recommended by Brammer, van Dokkum & Coppi (2008).

We require hosts to be isolated by excluding hosts that are within R_{200} of a galaxy with higher stellar mass and at the same redshift $(z - z_{host})/z_{host} < 0.007$. We estimate R_{200} from the stellar mass-to-halo mass relation from Dutton et al. (2010).

In total, COSMOS contains 3038 host galaxies between redshifts 0.1 and 0.8 which matched our criteria. Fig. 1 of N12 shows the stellar mass distribution in bins of redshift for COSMOS hosts. The deeper and narrower CANDELS has 1708 host galaxies between redshifts 0.4 and 1.5. Fig. 1 shows the stellar mass distribution of CANDELS hosts in bins of redshift.

2.2 CANDELS satellite candidate selection

We use the 3D-HST point spread function (PSF)-matched photometric catalogues to select the majority of satellite candidates. These catalogues were created with SourceExtractor (Bertin & Arnouts 1996, hereafter SE) on PSF-matched, variance-weighted mean-combined *F*160*W*, *F*140*W* and *F*125*W* images. Satellite candidates include all non-stellar[1] objects brighter than $F160W < 25$ AB magnitudes between $0.07 < R/R_{200,host} < 0.5$, where $R_{200,host}$ is estimated based on the host stellar mass and stellar mass-to-halo mass relation from equation 3 of Dutton et al. (2010) for early-type galaxies. The limit of $F160W < 25$ magnitude is chosen to ensure over 90 per cent detection completeness in both the CANDELS deep

[1] SE `CLASS_STAR` < 0.8 and 3D-HST `star_flag` !=1

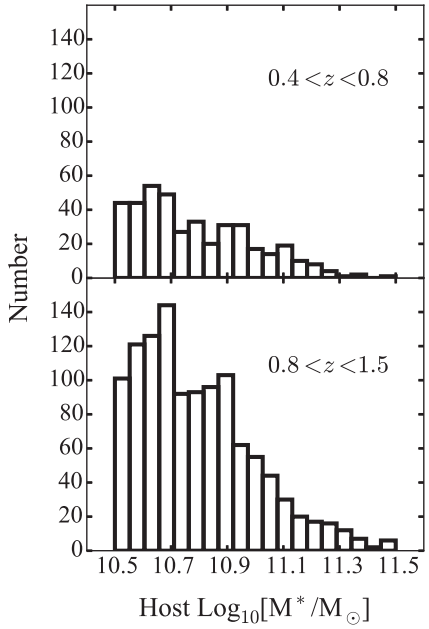

Figure 1. The stellar mass distribution of host galaxies in CANDELS divided into bins of redshift. Fig. 1 of N12 shows the corresponding distribution of host galaxies in COSMOS.

and wide imaging based on fig. 14 from Skelton et al. (2014), while the radial limits ensure accurate photometry near the host galaxies and a favourable ratio of satellites to background/foreground objects in the outer region.

As we demonstrated in Nierenberg et al. (2011, hereafter N11) and N12, even with deep, high-resolution *HST* imaging, photometric accuracy and completeness suffer within several effective radii of a bright central galaxy. To counter this, we empirically model and subtract the host light profile, and then perform our own object detection and photometry in small regions near the host galaxies, using SE parameters which match those used to create the 3D-HST catalogues. We then add the new object detections to the full 3D-HST catalogues, and update the photometry only for the region near the host galaxies. This method improves completeness and photometric accuracy very near the host galaxies (N11; N12). We perform the empirical host subtraction separately in both the detection image and in the *F*160*W* science image. We then apply the same empirical photometric correction to the *F*160*W* MAG_AUTOs as applied to make the 3D-HST photometric catalogues (see Skelton et al. 2014, fig. 10).

3 STATISTICAL ANALYSIS

We detect satellites statistically in monochromatic *F*160*W* data in CANDELS (*F*814 for COSMOS), as an increase in the number density of objects relative to the background/foreground number density measured outside of the host galaxy R_{200}. The statistical model framework is described in detail in N11 and N12. The measurement is made in two subdivided bins of host stellar mass $10.5 < \log_{10}[M_*/\mathrm{M}_\odot] < 11$, $11 < \log_{10}[M_*/\mathrm{M}_\odot] < 11.5$ and three bins of redshift $0.1 < z < 0.4$, $0.4 < z < 0.8$, $0.8 < z < 1.5$. Each redshift and host stellar mass bin is treated as an independent data set. Results for CANDELS and COSMOS are inferred separately. Model parameter definitions and priors are listed in Table 1 for CANDELS, and Table 1 in N12 for the COSMOS.

In brief, the number density of objects around the host galaxies is parametrized as the sum of a uniformly distributed number of background/foreground objects, and a population of satellite galaxies with a power-law spatial distribution with projected slope γ_p, such that $P(r_\mathrm{sat}) \propto r_\mathrm{sat}^{\gamma_\mathrm{p}}$.

In this work, we update the model relative to N11 and N12, by directly inferring the slope and bright end cutoff of the satellite luminosity function rather than iteratively inferring the cumulative number of satellites brighter than a fixed $\delta_\mathrm{m} = m_\mathrm{sat} - m_\mathrm{host}$, for a series of δ_m values. We model the luminosity function of satellites in units of δ_m as a Schechter function with faint end slope α_s and bright end cutoff of $\delta_\mathrm{m,o}$:

$$P(\delta_\mathrm{m,sat}|\alpha_\mathrm{s}, \delta_\mathrm{m,o}) \propto 10^{\frac{\alpha_\mathrm{s}+1}{2.5}(\delta_\mathrm{m,o}-\delta_\mathrm{m,sat})} \times \exp\left[-10^{(\delta_\mathrm{m,o}-\delta_\mathrm{m,sat})}\right]. \quad (1)$$

The total model number of satellites per host, $N_\mathrm{s,o}$, within $0.07 < r/R_{200} < 0.5$ is defined between $\delta_\mathrm{m,min,o}$ and $\delta_\mathrm{m,max,o}$, the minimum and maximum values respectively where the luminosity function can be measured reliably for the majority of the sample. These values vary depending on the average magnitude of the hosts in each redshift bin, as $\delta_\mathrm{m,max,o}$ for a given host is $25 - m_\mathrm{host}$; the satellite luminosity function of brighter hosts can be measured to lower values of δ_m. Table 1 gives the values of the limits $\delta_\mathrm{m,min,o}$ and $\delta_\mathrm{dm,max,o}$ selected for the inference in each host redshift and stellar mass bin.

We adopt non-uniform priors on the satellite spatial distribution, the background/foreground number density and the slope of the background/foreground luminosity function. In N12, we found that $\gamma_\mathrm{p} = -1.1 \pm 0.3$ over a wide range of redshifts, satellite luminosities and host stellar masses and morphologies, so for this work we adopt a Gaussian prior on γ_p with mean -1.1 and standard deviation 0.3. As we show in N12, adopting this prior does not affect the mean inferred number of satellites, but it does decrease the uncertainty,

Table 1. Model parameter definitions and priors.

Parameter	Description	Prior
$N_\mathrm{s,o}$	Integrated number of satellites with $\delta_\mathrm{m,min,o} < \delta_\mathrm{m} < \delta_\mathrm{m,max,o}$	U(0,100)[a]
α_s	Faint end slope of the satellite luminosity function (equation 1)	U(−2.9, 0)
$\delta_\mathrm{m,o}$	Bright cutoff of the satellite luminosity function (equation 1)	U(−8, 4)
γ_p	Projected satellite number density radial profile	G(−1.1, 0.3)[b]
Σ_b	Number of background/foreground galaxies per arcmin^2	Gaussian, varies with host mass, redshift and field
α_b	Slope of background/foreground magnitude number counts	G(0.28,0.01)

[a]U(min,max) is a uniform prior between the min and max values.
[b]G(mean, std) is a Gaussian prior defined by the mean and standard deviation.

Table 2. Inferred median and 1σ confidence intervals for the parameters defining the satellite luminosity function, in bins of host galaxy stellar mass and redshift. Parameters are defined in Table 1. The number of satellites is integrated within $0.07 < R/R_{200,\rm host} < 0.5$ where the mean value of $R_{200,\rm host}$, in units of kpc, is given in column 3 for each bin. Note that the normalization of the luminosity function $N_{\rm s,o}$, is defined over different intervals of $\delta_{\rm m} = m_{\rm sat} - {\rm m}_{\rm host}$ of the luminosity function for each of the bins to account for the fact that the completeness varies with redshift and host stellar mass. The minimum and maximum values for each bin are given in column 4.

$\log[M^*_{\rm host}/{\rm M}_\odot]$	$z_{\rm host}$	$\langle R_{200,\rm host}\rangle$	$\delta_{\rm m,min,o}$–$\delta_{\rm dm,max,o}$	$N_{\rm s,o}$	α_s	$\delta_{\rm m,o}$
10.5–11.0	0.4–0.8	196	3–6	2^{+1}_{-1}	$-1.4^{+0.6}_{-0.5}$	1^{+1}_{-4}
11.0–11.5	0.4–0.8	237	2–6	4^{+3}_{-3}	$-1.0^{+0.7}_{-0.7}$	2^{+1}_{-4}
10.5–11.0	0.8–1.5	290	2–4.5	$0.7^{+0.5}_{-0.4}$	$-0.7^{+0.5}_{-0.7}$	1^{+1}_{-1}
11.0–11.5	0.8–1.5	338	2–5	$2.5^{+0.9}_{-0.9}$	$-1.1^{+0.6}_{-0.5}$	1^{+1}_{-2}

and is useful for constraining the properties of satellites around the much smaller sample of CANDELS host galaxies.

We constrain the properties of the background/foreground galaxy in annuli outside of the region where we detect satellite galaxies. This method has been shown to accurately characterize the density of both random line-of-sight structure and correlated structure which is not gravitationally bound to the host galaxies (Chen 2008; Liu et al. 2011). We select annuli within $1 < R/R_{200,\rm host} < 2$ to measure both the background/foreground number density, $\Sigma_{\rm b}$, and the slope of the number counts $\alpha_{\rm b}$, where $N_{\rm b}(m) \propto \Sigma_{\rm b} 10^{\alpha_{\rm b} m}$. These values do not depend strongly on the choice of the annuli radius, given the measurement uncertainty. We include $\Sigma_{\rm b}$ and $\alpha_{\rm b}$ as model parameters with Gaussian priors with mean and standard deviations given by the values measured in the outer annuli. This enables us to directly account for the effects of measurement uncertainties in $\Sigma_{\rm b}$ and $\alpha_{\rm b}$ in the inferred satellite properties. The prior values for these parameters are listed in Table 1.

4 RESULTS

The inferred median values and 1σ uncertainties for the satellite luminosity function parameters in CANDELS are given in Table 2 for the four host stellar mass and redshift bins. For all host stellar mass and redshift regimes, the prior values for the projected number density radial profile of satellites $\gamma_{\rm p}$, the number density of foreground/background objects and the slope of the background/foreground number counts were recovered, with no tightening of the constraints. This was expected given that the prior on $\gamma_{\rm p}$ is derived from the much larger COSMOS sample, while the background/foreground number density is measured in a much larger region than the region in which satellite properties are inferred. Fig. 2 shows the inferred cumulative satellite luminosity function for CANDELS (dark hatched region) and COSMOS (black points) with satellite numbers extrapolated to be within $0.07 < r/R_{200,\rm host} < 1$ based on the inferred value of the slope of the satellite number density radial profile $\gamma_{\rm p}$.

For CANDELS, we plot in black regions which do not overlap with COSMOS, and which had a significant number of hosts (>10) with $\delta_{\rm m,\,max,\,i} = 25 - m_{\rm host}$, to ensure that the luminosity function is well constrained by the data. In light grey, we show the extrapolation of the luminosity function to fainter values of $\delta_{\rm m}$ where the data are less constraining, which is reflected in the increased uncertainty in the inferred luminosity function at these values. We also extrapolate the CANDELS results to brighter values of $\delta_{\rm m}$ to demonstrate the consistency with COSMOS results, and to show the overall shape of the luminosity function in the higher redshift bin. The number of satellites is well constrained and consistent with prior measurements of the luminosity function from COSMOS. N12 gives a detailed comparison between the lower redshift ($0.1 < z < 0.4$) COSMOS results and other results from the literature.

The inferred slope of the satellite luminosity function marginalized over all redshift and host stellar mass bins is $\alpha_{\rm s} \sim -1.1 \pm 0.3$, consistent within the measurement uncertainties for all the redshift and host stellar mass regimes. At lower redshift, the bright cutoff for CANDELS hosts is not well constrained owing to the small number of hosts and the low numbers of satellites per host near the bright end. At higher redshift, the bright cutoff is $\delta_{\rm m,o} \sim 1 \pm 1$ for both host stellar mass bins.

This result is broadly consistent within the measurement uncertainties with the low-redshift $z\sim$0.01–0.05 luminosity function measurement of satellites brighter than $M_r \sim -14$ from Lanet et al. (2015) which fit a double Schechter function to their satellites and found a slope of ~ -1 for satellites with absolute magnitudes brighter than -18 (corresponding to $\delta_{\rm m}$ values of $\sim$2–3 depending on host stellar mass), and slope of ~ -1.6 for satellites fainter than -18. Our result is also consistent with measurements of the slope of the stellar mass function of field galaxies and satellites between redshifts $\sim$0–4 which typically find values of α between -1 and -2 (e.g. Baldry et al. 2012; Santini et al. 2012; Duncan et al. 2014; Grazian et al. 2015; Lanet et al. 2015; Graus et al. 2016). Our data are not constraining enough to test whether satellite galaxies follow the field galaxy trend of decreasing α with increasing redshift.

It is interesting to compare these new high-redshift satellite observations with local observations of Milky Way-mass hosts. Assuming that the Milky Way has approximately doubled in stellar mass since $z \sim 1$ (e.g. Behroozi, Conroy & Wechsler 2010; Lehnert et al. 2014), Milky Way progenitors fall on the lower end of the lower stellar mass hosts in the redshift bin 0.8–1.5. Hosts in this stellar mass bin have $\sim 2 \pm 0.7$ satellite galaxies with $\delta_{\rm m} > 4$, and $\sim 0.8 \pm 0.3$ with $\delta_{\rm m} > 2$ corresponding to the present-day magnitude offsets between the Small Magellanic Cloud (SMC) and the Milky Way, and the Large Magellanic Cloud (LMC) and the Milky Way, respectively. This frequency is marginally higher, but still consistent within the measurement uncertainties, with low-redshift observations where Milky Way stellar mass hosts have about 0.3 ± 0.1 and 0.2 ± 0.1 SMCs and LMCs, respectively (see also Guo et al. 2011a; Lareset al. 2011; Liu et al. 2011).

5 COMPARISON WITH THEORETICAL MODELS

This new measurement of faint satellites provides a new constraint for models of galaxy formation. We compare our results with four theoretical predictions described below. Three of the predictions are from either semi-analytic or hydrodynamical models applied to CDM cosmologies, and the fourth prediction is a semi-analytic model applied to a WDM cosmology. We note that when varying the dark matter between warm and cold, we hold the star formation parameters fixed in order to explicitly demonstrate how varying the underlying dark matter with fixed star formation compares with

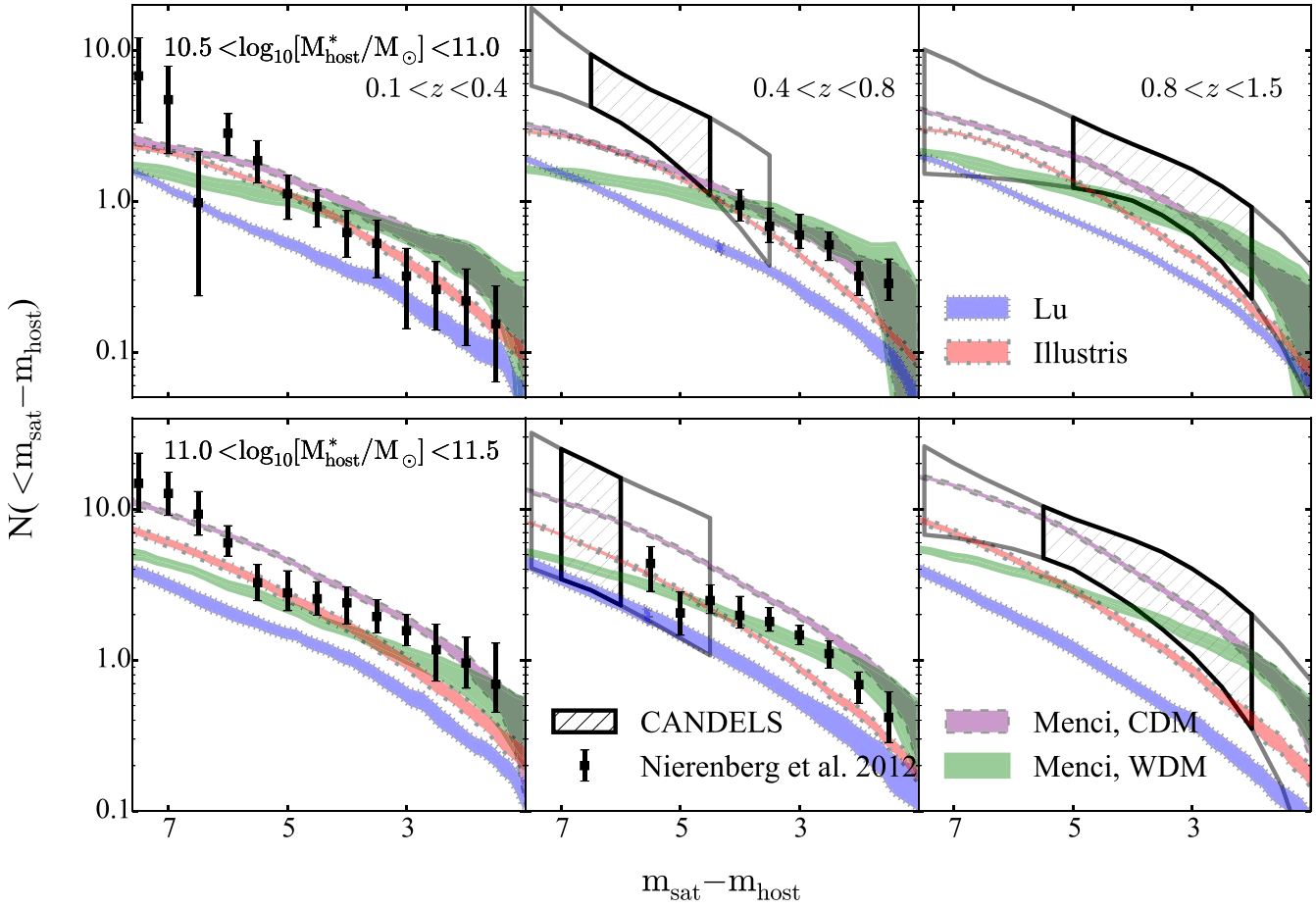

Figure 2. The cumulative luminosity function of satellite galaxies of hosts divided by bins of redshift (from left to right) and stellar mass (from top to bottom) within $0.07 < r/R_{200} < 1.0$. Black points with error bars and hatched region show the 1σ confidence interval from COSMOS $F1814W$ and CANDELS $F160W$ imaging, respectively. The black points and hatched region were used to compute χ^2 values for the comparison with theory, while the grey region represents extrapolations of the inferred luminosity function. Blue, purple and red lines are theoretical predictions with CDM from Lu et al. (2014), Menci et al. (2014) and Illustris (Vogelsberger et al. 2014b). The green luminosity function is the same star formation model as for the Menci CDM model, but applied to a WDM halo mass function (Menci et al. 2012).

varying between different star formation models with fixed dark matter.

5.1 Menci

The Menci model is a semi-analytic model applied to dark matter merging trees. We include a summary of the dark matter and semi-analytic models below; we refer the reader to Menci et al. (2014) for a detailed description.

In this work, we consider both a CDM and a WDM merging tree. Both models track subhaloes after they have entered the virial radius of the main halo, enabling them to coalesce with the central galaxy after orbital energy loss due to dynamical friction, merge with another subhalo or survive as a satellite halo. CDM halo merging trees are generated through a Monte Carlo procedure adopting the merging rates given by the extended Press–Schechter (see Lacey & Cole 1993) formalism. The WDM power spectrum is generated using the method described by Menci et al. (2012), with some modifications for the present work. First, we have included a sharp k filter to relate the power spectrum to the variance of density perturbations (see Benson et al. 2013; Schneider, Smith & Reed 2013). We assume a thermal relic mass $m_X = 1.5$ keV for the WDM candidate which yields a power spectrum corresponding to that produced by (non-thermal) sterile neutrinos with mass $m_{\rm sterile} \approx 6$–$12$ keV, depending on the production mechanism (see, e.g., Kusenko 2009; Destri, de Vega & Sanchez 2013). Indeed, these constitute the simplest candidates (see e.g. Abazajian 2014) for a dark matter interpretation of the origin of the recent unidentified X-ray line reported in stacked observations of X-ray clusters (Boyarsky et al. 2014; Bulbul et al. 2014). This particle mass is consistent with observational limits from ultra-faint dwarf galaxies (Lovell et al. 2012, 2014; Horiuchi et al. 2014), although still in tension with Lyman α forest constraints which yield $m_X \gtrsim 3.3$ keV (Viel et al. 2013). A discussion of the various uncertainties which may affect the constraints is given in Abazajian et al. (2011) and in Garzilli, Boyarsky & Ruchayskiy (2015). This mass is also in tension with recent results from Menci et al. (2016) based on the abundance of high-redshift galaxies $m_X > 2.1$ keV, 3σ confidence. We have chosen this relatively low particle mass to highlight the effect of suppressing the power spectrum, in comparison with varying baryonic physics models with fixed underlying CDM dark matter.

The processes affecting baryons are connected in the same way to the evolution of both CDM and WDM haloes. The baryonic model includes atomic cooling into rotationally supported discs

following Mo, Mao & White (1998). Star formation occurs quiescently over long time-scales (∼1 Gyr), and in bursts (∼1 Myr) triggered by galaxy interactions and disc instabilities. Star formation is suppressed via feedback from supernova and active galactic nuclei as described in Menci et al. (2008). The luminosity is computed by convolving the star formation histories of the galaxy progenitors with a synthetic spectral energy distribution, which we take from Bruzual & Charlot (2003) assuming a Salpeter initial mass function. The model includes tidal stripping of part of the stellar content of each satellite galaxy following Henriques & Thomas (2010).

5.2 Lu

The Lu model is a semi-analytic model applied to a set of halo merger trees extracted from a large cosmological *N*-body simulation, the Bolshoi Planck simulation, which is the same as the Bolshoi simulation (Klypin, Trujillo-Gomez & Primack 2011), but with a cosmology favoured by Planck data (Planck Collaboration XIII 2015) with parameters $\Omega_{\rm m,0} = 0.307\,11$, $\Omega_{\Lambda,0} = 0.692\,89$, $\Omega_{\rm b,0} = 0.048$, $h = 0.7$, $n = 0.96$ and $\sigma_8 = 0.82$. The mass resolution of the simulation allows the model to track haloes and subhaloes with mass $\sim 7 \times 10^9\,{\rm M}_\odot\,h^{-1}$. The prescriptions for the baryonic processes implemented in the Semi-Analytic Model are detailed in Lu et al. (2014). The model parameters governing star formation and feedback are tuned using a Markov chain Monte Carlo (MCMC) optimization to match the local galaxy stellar mass function (Moustakas et al. 2013). Therefore, it is guaranteed to produce a global galaxy stellar mass function for the stellar mass range between 10^9 and $10^{12}\,{\rm M}_\odot$ at redshift zero within the observational uncertainty for the given parametrization of the model.

5.3 Illustris

The Illustris simulation (Vogelsberger et al. 2014b) modelled a 106 Mpc^3 volume including both dark matter and baryons using the AREPO simulation code (Springel 2010b). The Illustris model includes a range of physical processes (including radiative gas cooling, star formation, stellar feedback and AGN feedback) that have been tuned to produce broad agreement with the cosmic star formation rate density and redshift $z = 0$ stellar mass function (Vogelsberger et al. 2013; Torrey et al. 2014). For a full description of the Illustris simulation setup, see Vogelsberger et al. (2014a) and Genel et al. (2014). The galaxy luminosities used here are assigned using the methods described in Torrey et al. (2015).

5.4 Comparison results

We compute the satellite luminosity function from the Lu and Illustris simulations by including all objects within $0.07 < R/R_{200} < 1$ of a host halo, where R_{200} is estimated using the same stellar mass-to-halo mass relation as was applied to the observations (Dutton et al. 2010). We note that the number of objects within R_{200} is significantly lower than the total number of subhaloes identified by the Friends-of-Friends algorithm for both Illustris and Lu models. However, the number does not depend strongly on whether the Dutton et al. (2010) relation is used to estimate the host virial radius, or whether the simulation value of $R_{\rm vir}$ is directly used. Satellites in the Menci merging tree simulations are identified based on host virial radius in a way similar to that of observations. Although we cannot directly exclude satellites within the central 0.07 R_{200} from the Menci model satellite counts, we can estimate the impact of excluding this volume by assuming that the satellites approximately follow the spatial distribution of the host dark matter plus light distribution, which is approximately isothermal in the interior of the halo. Under the conservative assumption that satellites exist to R of zero, implying that the host occupies no volume, we find that excluding the central 0.07 R_{200} reduces the number of satellites by ∼5 per cent, which we include as an additional model uncertainty when comparing with the data. This estimate assumes that all satellites follow the same spatial distribution regardless of mass, which is consistent with observations over the mass range considered here (N12).

For the Lu and Illustris models, hosts are selected with the same isolation criteria as was applied to the observation. We have tested that in the case of the *N*-body simulations, using the observational isolation criteria to select hosts yields a consistent result with selecting hosts based on simulation definitions of central versus satellite galaxy; thus, for the Menci CDM and WDM merging trees, which lack spatial information, we directly use the simulation definition of host versus satellite.

We compute the scatter in the theoretical predictions due to the finite sample size of the observations by bootstrap resampling a subset of the theoretical host–satellite systems in samples equal to the number of data hosts in the data for each redshift and host stellar mass range. This scatter is then incorporated with the measurement uncertainty in the data when computing chi-squared values.

We compute the χ^2 between the model number of satellites per host and the measured numbers as a function of δ_m, for discrete values of $\delta_{\rm m}$ spaced in intervals of 0.5 for COSMOS data and 1 for CANDELS data. In regions where both CANDELS and COSMOS data overlapped, the COSMOS data are used in the comparison with theory owing to its higher precision. Although our data are composed of measurements in both $F814W$ and $F160W$, the luminosity function of satellites as a function of $\delta_{\rm m} = m_{\rm sat} - {\rm m}_{\rm host}$ does not have a significant dependence on observed band in any of the theoretical models for redshifts <0.8.

We include the covariance between data points in our χ^2 estimate, which is significant owing to the fact that we are considering the cumulative numbers of satellites, and thus the same host galaxy will contribute to the number of satellites in multiple bins. The covariance matrix between data points was computed using 2500 draws from the MCMC results for CANDELS while for COSMOS it was computed by bootstrap resampling the input data and re-inferring the satellite numbers. The black hatched region of the CANDELS measurement shows the range of CANDELS data which was used to compute the χ^2.

Table 3 lists the χ^2 values between the models and observed luminosity for each bin in host stellar mass and redshift, along with the corresponding number of data points. The χ^2 values were 68, 47 and 81 for the Menci, Illustris and Lu CDM models, and 49 for the Menci WDM model for 53 degrees of freedom. Accounting for the number of degrees of freedom, the χ^2 goodness-of-fit test gives an approximately ∼20 per cent, 90 per cent, 1 per cent and 70 per cent chance that the data were drawn from each model respectively. These values are approximately equivalent, with the Lu and Menci CDM models being somewhat disfavoured relative to the others, and the Illustris CDM and Menci WDM models performing the best.

6 DISCUSSION

These data provide an important new constraint for models of satellite galaxy formation and evolution. While overall there is not a strong preference for a particular model, it is interesting to consider

Table 3. Model χ^2 values, after accounting for covariance in the data, for each host stellar mass and redshift bin. We note that a continuous luminosity function is inferred by CANDELS data, but to compare with predictions from simulations we sample the luminosity function values at discreet points spaced every 0.5 δ_m within the dark hatched region of Fig. 2.

z	$\log_{10}[M^*_{host}/M_\odot]$	No. of data points	Menci CDM	Menci WDM	Lu	Illustris
0.1–0.4	10.5–11.0	13	15	15	11	9
	11.0–11.5	13	13	10	17	9
0.4–0.8	10.5–11.0	9	4	6	18	8
	11.0–11.5	11	29	7	27	17
0.8–1.5	10.5–11.0	4	1	1	4	3
	11.0–11.5	4	1	2	3	1
Total		54	63	41	81	47

how the models performed in the different regimes. In particular, the Menci WDM model provides the best overall match to the luminosity function around higher mass hosts while the Lu and Illustris models match the luminosity function of low-mass hosts at low redshifts. There is some tension between the numbers of faint satellites in the redshift range 0.4–0.8 for lower stellar mass hosts, for all of the models, which somewhat underestimate the slope of the satellite luminosity function. Overall, models which produce accurate predictions for Milky Way-mass hosts at low redshifts tend to underestimate the number satellite galaxies found around those hosts at higher redshifts and at higher stellar masses, and vice versa.

This measurement provides a complimentary constraint on the models to constraints from measurements of field galaxy properties. In particular, the Illustris and Menci CDM models both significantly overpredict the number of low-mass $\log_{10}M_*/M_\odot < 10$ field galaxies at redshift zero by a factor of ∼3–5 (Menci et al. 2012; Genel et al. 2014; Vogelsberger et al. 2014a). While stronger feedback might resolve this discrepancy, it would lead to a further suppression of the satellite luminosity function relative to observation, in the case of Illustris. The Lu model matches the field luminosity function well at redshift zero but tends to underpredict the slope of the luminosity function at higher redshift (Lu et al. 2014). As shown in Lu et al. (2014), the model also underestimates the metallicities of low-mass galaxies owing to the strong feedback implementation. One possible solution to these discrepancies in the context of a CDM cosmology may be in the form of an alternative feedback model such as the preventative feedback model of Lu, Mo & Wechsler (2015), in which star formation is suppressed due to the pre-heated intergalactic medium, rather than via ejective feedback processes such as outflows. This mode of suppression better reproduces the observed cold gas fractions, star formation histories and sizes of low-mass galaxies for field galaxies, although it has yet to be tested for satellite galaxies. Preventative feedback may also impact the simulated mass–metallicity relation by reducing fraction of metals that are ejected from the galaxy (Zahid et al. 2014).

An interesting result of this comparison is that the variation between the predicted luminosity function in CDM models with different star formation models is as great as the variation between the CDM and WDM models with fixed star formation. In a future work, it would be interesting to compare observational results with a broader range of dark matter models such as those generated by ETHOS (Cyr-Racine et al. 2016; Vogelsberger et al. 2016). A direct measurement of the low-mass halo mass function via gravitational lensing would provide a powerful constraint for these dark matter models (Treu 2010, and references therein) and therefore play an important role in constraining the star formation physics in low-mass haloes. In order to understand how luminous satellites populate the subhaloes detected in gravitational lensing studies, it is important to study luminous satellites around gravitational-lens stellar mass hosts (see also Nierenberg, Oldenburg & Treu 2013a; Fiacconi et al. 2016).

7 SUMMARY

Using CANDELS *F*160*W* imaging, we measure the luminosity function of faint satellites around hosts with stellar masses within $10.5 < \log_{10}M_*/M_\odot < 11.5$ to a redshift of 1.5. The deep imaging enables us to detect satellites with $\delta_m = m_{sat} - m_{host} = 4$ (fainter than the SMC) to an unprecedented redshift of 1.5, and to detect $\delta_m = 7$ satellites between redshifts 0.4 and 0.8. We combine these new results with lower redshift (0.1–0.8) measurements from *F*814 COSMOS imaging from N12. We compare these results to predictions from four theoretical models (Menci et al. 2012, 2014; Lu et al. 2014; Vogelsberger et al. 2014a). While none of the models was definitively ruled out, different models matched the observations more or less well in different regimes of redshift and host stellar mass, which highlights the value of this data set in distinguishing between models which performed similarly at redshift zero around Milky Way-mass host galaxies. These data provide important new constraining power for future implementations of feedback and dark matter physics in these models.

Our conclusions are summarized as follows.

(i) We infer the parameters of the satellite luminosity function faint end slope to be $\alpha_s = -1.1 \pm 0.3$, consistent over all redshift and stellar host stellar mass bins within the measurement uncertainties. We find that the bright cutoff relative to the host magnitude is not well constrained within $0.4 < z < 0.8$ for CANDELS hosts, and is $\delta_{m,o} \sim 1 \pm 1$, for $0.8 < z < 1.5$.

(ii) We detect SMC-luminosity satellite galaxies to a redshift of 1.5, and find that Milky Way-like progenitors at redshift ∼1 have consistent numbers of LMC/SMC analogues with redshift zero galaxies. In general, the cumulative number of satellites per host as a function of the offset between host and satellite magnitude is constant as a function of redshift within the measurement uncertainties, but is higher for hosts with higher stellar masses.

(iii) The theoretical models varied in their ability to predict the satellite luminosity function in different regimes of host stellar mass and redshift. The models performed similarly overall; however, models which fit the luminosity function of the satellites of low

stellar mass hosts tended to underpredict the number of satellites around higher stellar mass hosts and vice versa. Future predictions will need an adjusted implementation of stellar feedback as a function of host stellar mass and redshift in order to resolve this discrepancy.

ACKNOWLEDGEMENTS

We thank Quan Guo for very helpful comments. We also thank R. Skelton and I. Momcheva for very helpful discussions and support with the 3D-HST data. Support for this work was provided by NASA through grant number HST-AR 13732 from the Space Telescope Science Institute, which is operated by AURA, Inc., under NASA contract NAS 5-26555.

The Bolshoi and MultiDark simulations have been performed within the Bolshoi project of the University of California High-Performance AstroComputing Center (UC-HiPACC) and were run at the NASA Ames Research Center. The MultiDark-Planck (MDPL) and the BigMD simulation suite have been performed in the Supermuc supercomputer at LRZ using time granted by PRACE.

PT acknowledges support from NASA ATP Grant NNX14AH35G. PT and MV acknowledge support through an MIT RSC award. The Illustris simulation was run on the CURIE supercomputer at CEA/France as part of PRACE project RA0844, and the SuperMUC computer at the Leibniz Computing Centre, Germany, as part of project pr85je. The analysis presented in this paper was run on the Harvard Odyssey and CfA/ITC clusters and though allocation TG-AST150059 granted by the Extreme Science and Engineering Discovery Environment (XSEDE) supported by the NSF.

REFERENCES

Abazajian K. N., 2014, Phys. Rev. Lett., 112, 161303
Abazajian K. N. et al., 2011, Astropart. Phys., 35, 177
Baldry I. K. et al., 2012, MNRAS, 421, 621
Behroozi P. S., Conroy C., Wechsler R. H., 2010, ApJ, 717, 379
Benson A. J. et al., 2013, MNRAS, 428, 1774
Bertin E., Arnouts S., 1996, A&AS, 117, 393
Boyarsky A., Ruchayskiy O., Iakubovskyi D., Franse J., 2014, Phys. Rev. Lett., 113, 251301
Brammer G. B., van Dokkum P. G., Coppi P., 2008, ApJ, 686, 1503
Brammer G. B. et al., 2012, ApJS, 200, 13
Brooks A. M., Kuhlen M., Zolotov A., Hooper D., 2013, ApJ, 765, 22
Bruzual G., Charlot S., 2003, MNRAS, 344, 1000
Bulbul E., Markevitch M., Foster A., Smith R. K., Loewenstein M., Randall S. W., 2014, ApJ, 789, 13
Chen J., 2008, A&A, 484, 347
Colombi S., Dodelson S., Widrow L. M., 1996, ApJ, 458, 1
Cyr-Racine F. Y., Sigurdson K., Zavala J., Bringmann T., Vogelsberger M., Pfrommer C., 2016, Phys. Rev. D., 93, 123527
Destri C., de Vega H. J., Sanchez N. G., 2013, Phys. Rev. D, 88, 083512
Duncan K. et al., 2014, MNRAS, 444, 2960
Dutton A. A., Conroy C., van den Bosch F. C., Prada F., More S., 2010, MNRAS, 407, 2
Fiacconi D., Madau P., Potter D., Stadel J., 2016, ApJ, 824, 144
Garzilli A., Boyarsky A., Ruchayskiy O., 2015, preprint (arXiv:e-prints)
Genel S. et al., 2014, MNRAS, 445, 175
Gnedin N. Y., 2000, ApJ, 535, L75
Graus A. S., Bullock J. S., Boylan-Kolchin M., Weisz D. R., 2016, MNRAS, 456, 477
Grazian A. et al., 2015, A&A, 575, A96
Grogin N. A. et al., 2011, ApJS, 197, 35
Guo Q., Cole S., Eke V., Frenk C., 2011a, MNRAS, 417, 370
Guo Q. et al., 2011b, MNRAS, 413, 101
Henriques B. M. B., Thomas P. A., 2010, MNRAS, 403, 768
Horiuchi S., Humphrey P. J., Oñorbe J., Abazajian K. N., Kaplinghat M., Garrison-Kimmel S., 2014, Phys. Rev. D, 89, 025017
Ilbert O. et al., 2009, ApJ, 690, 1236
Kaufmann T., Bullock J. S., Maller A., Fang T., 2008, in Minchin R., Momjian E., eds, AIP Conf. Ser. Vol. 1035, The Evolution of Galaxies Through the Neutral Hydrogen Window. Am. Inst. Phys., New York, p. 147
Klypin A., Kravtsov A. V., Valenzuela O., Prada F., 1999, ApJ, 522, 82
Klypin A. A., Trujillo-Gomez S., Primack J., 2011, ApJ, 740, 102
Koekemoer A. M. et al., 2011, ApJS, 197, 36
Kusenko A., 2009, Phys. Rep., 481, 1
Lacey C., Cole S., 1993, MNRAS, 262, 627
Lan T.-W., Ménard B., Mo H., 2016, MNRAS, 459, 3998
Lares M., Lambas D. G., Domínguez M. J., 2011, AJ, 142, 13
Lehnert M. D., Di Matteo P., Haywood M., Snaith O. N., 2014, ApJ, 789, L30
Lilly S. J. et al., 2007, ApJS, 172, 70
Liu L., Gerke B. F., Wechsler R. H., Behroozi P. S., Busha M. T., 2011, ApJ, 733, 62
Lovell M. R. et al., 2012, MNRAS, 420, 2318
Lovell M. R., Frenk C. S., Eke V. R., Jenkins A., Gao L., Theuns T., 2014, MNRAS, 439, 300
Lu Y., Mo H. J., Katz N., Weinberg M. D., 2012, MNRAS, 421, 1779
Lu Y. et al., 2014, ApJ, 795, 123
Lu Y., Mo H. J., Wechsler R. H., 2015, MNRAS, 446, 1907
Macciò A. V., Kang X., Fontanot F., Somerville R. S., Koposov S., Monaco P., 2010, MNRAS, 402, 1995
Menci N., Rosati P., Gobat R., Strazzullo V., Rettura A., Mei S., Demarco R., 2008, ApJ, 685, 863
Menci N., Fiore F., Lamastra A., 2012, MNRAS, 421, 2384
Menci N., Gatti M., Fiore F., Lamastra A., 2014, A&A, 569, A37
Menci N., Grazian A., Castellano M., Sanchez N. G., 2016, MNRAS, 825, L1
Mo H. J., Mao S., White S. D. M., 1998, MNRAS, 295, 319
Moore B., Ghigna S., Governato F., Lake G., Quinn T., Stadel J., Tozzi P., 1999, ApJ, 524, L19
Moustakas J. et al., 2013, ApJ, 767, 50
Newman A. B., Ellis R. S., Bundy K., Treu T., 2012, ApJ, 746, 162
Nierenberg A. M., Auger M. W., Treu T., Marshall P. J., Fassnacht C. D., 2011, ApJ, 731, 44 (N11)
Nierenberg A. M., Auger M. W., Treu T., Marshall P. J., Fassnacht C. D., Busha M. T., 2012, ApJ, 752, 99 (N12)
Nierenberg A. M., Oldenburg D., Treu T., 2013a, MNRAS, 436, 2120
Nierenberg A. M., Treu T., Menci N., Lu Y., Wang W., 2013b, ApJ, 772, 146
Oke J. B., 1974, ApJS, 27, 21
Papastergis E., Martin A. M., Giovanelli R., Haynes M. P., 2011, ApJ, 739, 38
Planck Collaboration XIII 2015, preprint (arXiv:e-prints)
Ruiz P., Trujillo I., Mármol-Queraltó E., 2015, MNRAS, 454, 1605
Sales L. V. et al., 2015, MNRAS, 447, L6
Santini P. et al., 2012, A&A, 540, A109
Schneider A., Smith R. E., Reed D., 2013, MNRAS, 433, 1573
Scoville N. et al., 2007, ApJS, 172, 38
Skelton R. E. et al., 2014, ApJS, 214, 24
Springel V., 2010a, ARA&A, 48, 391
Springel V., 2010b, MNRAS, 401, 791
Starkenburg E. et al., 2013, MNRAS, 429, 725
Strigari L. E., Wechsler R. H., 2012, ApJ, 749, 75
Tal T., Quadri R. F., Muzzin A., Marchesini D., Stefanon M., 2014, preprint (arXiv:e-prints)
Thoul A. A., Weinberg D. H., 1996, ApJ, 465, 608
Torrey P., Vogelsberger M., Genel S., Sijacki D., Springel V., Hernquist L., 2014, MNRAS, 438, 1985
Torrey P. et al., 2015, MNRAS, 447, 2753
Treu T., 2010, ARA&A, 48, 87

Viel M., Becker G. D., Bolton J. S., Haehnelt M. G., 2013, Phys. Rev. D, 88, 043502
Vogelsberger M., Genel S., Sijacki D., Torrey P., Springel V., Hernquist L., 2013, MNRAS, 436, 3031
Vogelsberger M. et al., 2014a, MNRAS, 444, 1518
Vogelsberger M. et al., 2014b, Nature, 509, 177
Vogelsberger M., Zavala J., Cyr-Racine F. Y., Pfrommer C., Bringmann T., Sigurdson K., 2016, MNRAS, 460, 1399
Wang W., White S. D. M., 2012, MNRAS, 424, 2574
Wetzel A. R., Hopkins P. F., Kim J.-h., Faucher-Giguère C.-A., Kereš D., Quataert E., 2016, MNRAS, 827, L23
Zahid H. J., Torrey P., Vogelsberger M., Hernquist L., Kewley L., Davé R., 2014, Ap&SS, 349, 873
Zolotov A. et al., 2012, ApJ, 761, 71

This paper has been typeset from a TEX/LATEX file prepared by the author.